Single field-of-view tomographic imaging of 3D impurity emission distribution in magnetized edge plasma of LHD

Single field-of-view tomographic imaging of 3D impurity emission distribution in magnetized edge plasma of LHD

Taisuke Kobayashi, Masahiro Kobayashi, Naofumi Iwama, et al.

View Online   Export Citation   CrossMark

ARTICLES YOU MAY BE INTERESTED IN

Space-resolved visible spectroscopy for two-dimensional measurement of hydrogen and impurity emission spectra and of plasma flow in the edge stochastic layer of LHD
Review of Scientific Instruments **88**, 033501 (2017); https://doi.org/10.1063/1.4976963

Development of a dual beamlet monitor system for negative ion beam measurements
Review of Scientific Instruments **89**, 123303 (2018); https://doi.org/10.1063/1.5056260

Optimized tomography methods for plasma emissivity reconstruction at the ASDEX Upgrade tokamak
Review of Scientific Instruments **87**, 123505 (2016); https://doi.org/10.1063/1.4971367
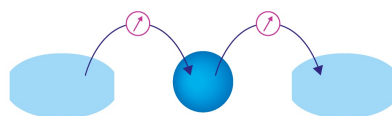
Single field-of-view tomographic imaging of 3D impurity emission distribution in magnetized edge plasma of LHD

Taisuke Kobayashi,[1] Masahiro Kobayashi,[1,2] Naofumi Iwama,[2] Arseniy Kuzmin,[2] Motoshi Goto,[1,2] and Gakushi Kawamura[1,2]

[1]*SOKENDAI (The Graduate University for Advanced Studies), 322-6 Oroshi-cho, Toki 509-5292, Japan*
[2]*National Institute for Fusion Science, National Institutes of Natural Sciences, 322-6 Oroshi-cho, Toki 509-5292, Japan*

A new tomographic scheme is proposed for reconstructing three dimensional (3D) impurity emission distributions from two dimensional (2D) measurements with a single field-of-view in the magnetized edge plasma in a Large Helical Device (LHD). The 2D image is obtained with a multi-channel fiber array spectrometer, which views the entire region of the edge stochastic magnetic layer of LHD, including divertor plates, divertor legs, the stochastic layer, and the last closed flux surface. The scheme introduces new regularization terms in the Lagrangian function, based on the transport feature in magnetized plasma that the transport parallel to the magnetic field lines is much faster than the transport across the magnetic field, thus assuming smooth distribution in the parallel direction. The scheme is benchmarked with the test data of 3D distribution in the measurement volume, where the effectiveness of the various regularization terms is surveyed and feasibility of the scheme is confirmed. The new scheme is applied to the experimental data in LHD for carbon impurity emissions of C^{1+} and C^{3+}, where the obtained distributions are discussed taking into account the plasma wall interaction and charge dependence of ionization potentials. *Published by AIP Publishing.*
https://doi.org/10.1063/1.5048218

I. INTRODUCTION

In magnetically confined fusion devices, understanding impurity transport in the edge region is a critical issue for controlling impurity radiation in the divertor region as well as impurity influx into the confinement region. Because of the very fast transport of charged particles parallel to magnetic field lines, the resulting impurity distributions are largely affected by magnetic field structure.[1]

LHD (Large Helical Device) is a heliotron type device, in which the magnetic field configuration is inherently non-axisymmetric.[2] The edge region is called the stochastic magnetic layer, where magnetic islands with different mode numbers overlap each other to induce chaotic field line trajectories. In this region, strong poloidal and toroidal asymmetry of impurity emission is predicted by plasma transport simulations.[3,4] Two-dimensional (2D) emission distribution measurements have been conducted so far with spectrometers in the edge region of LHD in order to study the relation between plasma transport and magnetic field structure.[5–7] However, the detailed comparison between the measured impurity emission and the magnetic field structure has been limited because of the line integration effect along the line of sight (LOS).

In this paper, we propose a new tomographic scheme to reconstruct three dimensional (3D) impurity emission distribution from single field of view 2D measurement in magnetized plasma by redistributing the signal along the line of sight. For this purpose, we utilize a characteristic of the magnetized plasma, where the plasma transport parallel to the magnetic field line is much faster than the plasma transport perpendicular

to magnetic field lines. The scheme is useful not only for helical devices with the complex magnetic field structure but also for tokamaks in the case of a limited number of observation ports.

The paper is organized as follows. In Sec. II, the experimental setup of the spectroscopy system as well as the magnetic field structure of LHD is explained. In Sec. III, the tomographic scheme is described with various regularization methods tested and its feasibility is discussed. The scheme is applied to the experimental data in Sec. IV. The paper is summarized in Sec. V.

II. EXPERIMENTAL SETUP

The relation between the viewing area of the spectrometer and the LHD torus is shown in Fig. 1. The open field lines in the edge region go around the torus along the helical coils until they are terminated by the divertor plates. The trajectories of the field lines are also shown in Fig. 1 in red and yellow. The spectrometer views the plasma from the outboard side. The line of sight (LOS) is inclined toward the top of the torus and toward the toroidal direction such that the LOS is almost tangential to the edge magnetic field lines. Figure 2 shows the field of view of the spectrometer, where 131 optical fibers are distributed to spatially resolve the edge region. The viewing area covers the last closed flux surface (LCFS), divertor legs, X-point, and divertor plates. The groups of red and yellow lines in Fig. 2 indicate divertor leg field lines; each group is connected to the different divertor plate arrays.
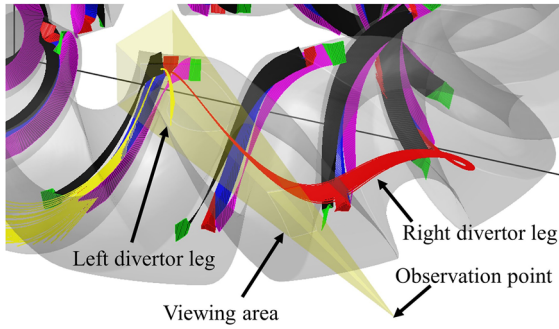
FIG. 1. The viewing area of the spectrometer shaded by yellow (quadrangular pyramid). The divertor leg field lines are shown with yellow and red lines. The divertor plate arrays at the inboard side are shown with black and pink surfaces. The vacuum vessel shape is shown in transparent gray.
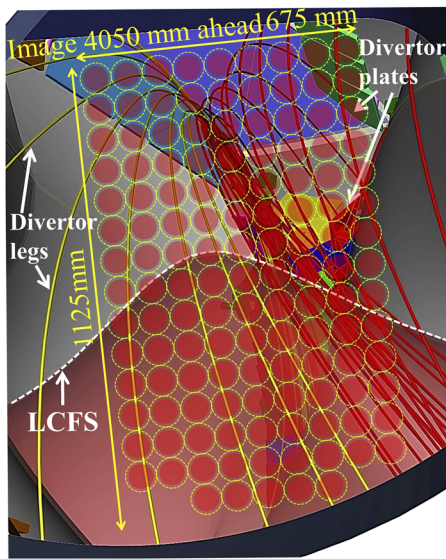

FIG. 2. Field of view and fiber distribution for the two-dimensional measurement. Yellow and red lines represent divertor legs, and the dashed line indicates the LCFS.

At the entrance slit of the spectrometer, the optical fibers are vertically aligned with a separation of 150 μm between each other. The image of the fibers is focused at the exit slit, where a charge coupled device (CCD) camera is equipped.

In order to obtain good focus of the fiber image in the wide area on the CCD detector, astigmatism is suppressed by introducing toroidal and spherical mirrors in the spectrometer. The detail of the optics of the spectroscopy system is described in Ref. 8. The spectrometer can change diffraction gratings remotely between 150, 300, and 2400 grooves/mm. In the present measurements, the grating of 150 grooves/mm is used for measurements of CII ($1s^2 2s 2p 3s$ $^4P^o$-$1s^2 2s 2p 3p$ ^4P, 514 nm), and the grating of 2400 grooves/mm is used for CIII ($1s^2 2s 3s$ ^3S-$1s^2 2s 3p$ $^3P^o$, 465 nm) and CIV ($1s^2 5f$ $^2F^o$-$1s^2 6g$ ^2G, $1s^2 5g$ ^2G-$1s^2 6h$ $^2H^o$, 466 nm). The wavelength resolutions near the center of the CCD are 1.07 nm and 0.06 nm with the gratings of 150 and 2400 grooves/mm, respectively. Exposure time and cycle time are set to 0.09-0.19 s and 0.2-0.3 s, respectively. These settings were changed depending on the gratings and the plasma parameters.

III. TOMOGRAPHY SCHEME

A. Field-line aligned 3D grid generation

For the present tomography scheme, we make use of the plasma transport feature that the transport is much faster along magnetic field lines as compared to the transport perpendicular to the field lines, which leads to smooth distribution of physical quantity along the magnetic field lines. In order to incorporate this effect in the projection matrix and in the regularizations of the tomographic inversion, the voxellation of the measurement volume is made such that the vertices of voxels are aligned along magnetic field lines.

Figure 3 shows the 2D distributions of the magnetic field line connection length (L_C) at different cross sections perpendicular to the LOS. L_C is defined as a length of the field line trajectory between divertor plates. The length labels in each panel in Fig. 3 (also Figs. 4, 6, and 10 below) show the distance from the observation point to the cross section, L_{dp}. The region in red represents L_C more than 10^4 m, which corresponds to a confinement region. Around the confinement region, the so-called stochastic magnetic field layer is formed, where regions with different L_C's (yellow, green, and blue) are mixed. L_C rapidly decreases in the radially outward direction as seen in the change of the color in the figure. Two divertor legs are visible with blue thin lines, and they cross each other at the
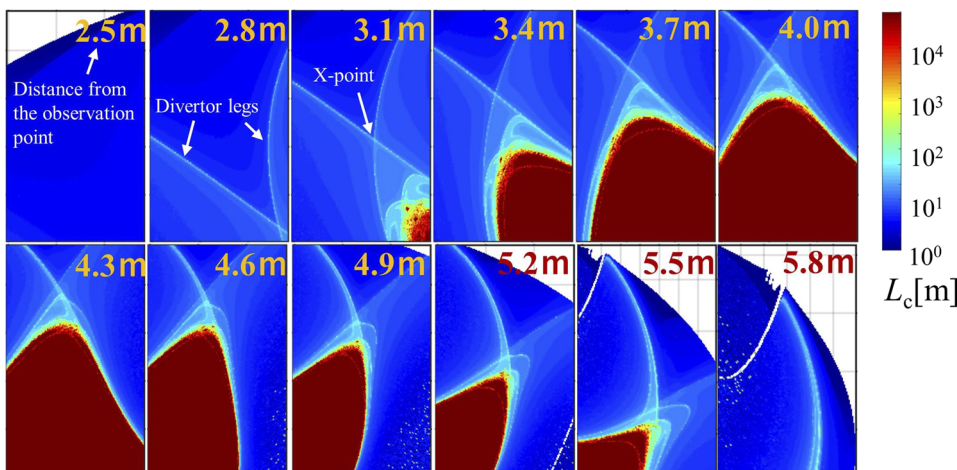

FIG. 3. Connection length (L_C) distribution in cross sections perpendicular to LOS. Length in each panel indicates the distance from the observation point. Two divertor legs are visible with blue thin lines, and they cross each other at the X-point.
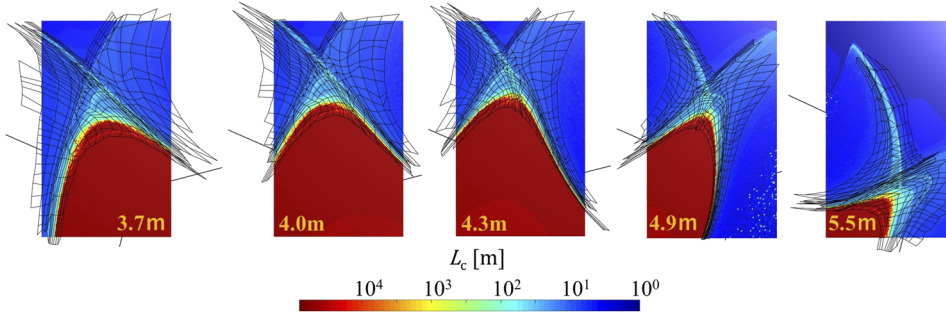
FIG. 4. Field-aligned 3D grid constructed for tomography: cross-sectional illustrations with the label L_{dp}. Vertices are aligned along the magnetic field lines.

X-point. (The color of the divertor legs in Figs. 1 and 2 is not relevant to the L_C but are only for visualization.)

The preparation of voxels for the projection matrix has been performed taking into account these magnetic field structures. The grid starts from the region just inside of LCFS and extends radially outward along the divertor legs, as shown in Fig. 4. This selection of grid area is based on possible emission areas of CII, CIII, and CIV, whose ionization potentials are 24.4, 48.0, and 64.7 eV, respectively, so that they rarely emit inside LCFS, where the temperature is usually higher than a few hundred eV. It is also considered that in the deep blue region in Fig. 3, where the L_C is less than 5 m, the plasma density is so low that impurity emission (except for neutrals) is very weak. The grid is first constructed at 4.0 m from the observation point. Then each vertex of the grid is traced along magnetic field lines to construct the 3D grid structure, in order to cover the region of $L_{dp} = 2.8$–5.7 m. The flux tube cross section in the edge region is strongly deformed along the magnetic field due to magnetic shear. Therefore, the grid was carefully constructed not to be crushed during the tracing, taking into account the magnetic field structure. At first, the very fine grid (typical size of 51 mm, and minimum size of 1.3 mm) was constructed to accommodate the strong deformation. Then the neighboring voxels having similar L_C within one order of magnitude are unified in order to reduce the number of voxels as much as possible to remedy the ill condition in tomographic inversion. There is, however, a region, where the field lines with different L_C's by several orders of magnitudes co-exist within a few mm in a radial direction. In such a region, the voxels with different L_C's more than one order are unified, anticipating that the perpendicular plasma transport smears out such fine structure. The criterion for the tomography voxel construction in the magnetized plasma still has to be studied carefully with a more refined measurement system and with a fine grid structure to find out a tolerable resolution of the grid. Eventually, in the present analysis, 1464 voxels in the entire measurement volume, which consists of 242 flux tubes, are constructed successfully, as shown in Fig. 4. The resulting spatial resolution of the grid along the line of sight is 30 cm. With this non-uniform voxellation, the elements $L_{m,k}$ of the projection matrix **L** in image analysis below are evaluated as

$$L_{m,k} = V_{m,k}/A_{m,l}, \tag{1}$$

where m and k are the indices of the optical fibers and the tomography voxels in the measurement domain, respectively. l is the index of each cross section perpendicular to the line of sight. Then, $V_{m,k}$ is the k-th voxel volume in the field of view

of the m-th fiber, and $A_{m,l}$ is the area in the l-th cross section covered by the field of view of the m-th fiber. The schematic of the voxel structure together with the indexes is shown in Fig. 5.

B. Regularization operators and solution

Using the provided **L**, an unknown vector **E** which represents the spatial distribution of emissivity in measurement volume is related to a data vector **S** which represents the observed image at the detector as follows:

$$\mathbf{LE} = \mathbf{S}. \tag{2}$$

The size of **E** is the number of voxels K = 1464, while the size of **S** is the number of fibers M = 131. $L_{m,k}$ in Eq. (1) is the contribution rate of the voxel value E_k to the output S_m. With the under-determined equation (2) (K > M), the inverse problem to obtain **E** from **S** will be ill-conditioned as is often the case in plasma imaging and especially in our experiment with a single field-of-view. In order to obtain a good solution, an appropriate regularization is required.

In the least-squares approach, a well-known strategy is to solve the problem in the scheme of minimization under constraint, which is reduced to minimizing Lagrangian functions of the form

$$\Lambda(E) = \frac{1}{M}\|\mathbf{LE} - \mathbf{S}\|^2 + \text{regularization terms,}$$

where $\|\mathbf{a}\|$ denotes the norm of vector **a**. A variety of regularization terms that lead to linear and nonlinear solutions have
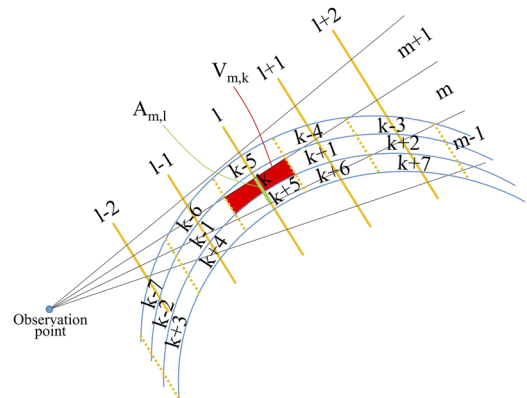

FIG. 5. Schematics of the structure of voxels and index used for the tomography, as an example of 5 voxels along field lines. k, m, and l represent the index of voxel, the optical fiber, and the cross section perpendicular to the line of sight, respectively.

been investigated in plasma imaging, which is usually given a strong limitation in the number of fields of view. When applied to plasma imaging, a notable feature is to use derivative operators, which are effective for smooth plasma profiles. Studies in the L2-norm regularizations of the Tikhonov type[9–13] and a modified type[14,15] and nonlinear regularizations of the Fisher type[16–19] and Hopfield neural net[20] are typical studies. In Ref. 18, an anisotropic derivative operator was applied and examined for 2D tomography in JET. The use of the anisotropic operator in velocity space was studied for fast-ion diagnostics in Ref. 21.

In the present analysis, within the Tikhonov scheme, we introduce a new anisotropic regularization, taking into account the transport feature of the magnetized plasma which should have distribution smoothed along flux tubes, as described in Sec. III A. That is, we define $\Lambda(\mathbf{E})$ as

$$\Lambda(\mathbf{E}) = \frac{1}{M}\|\mathbf{LE} - \mathbf{S}\|^2 + \gamma_1\|\mathbf{D}_1\mathbf{E}\|^2 + \gamma_2\|\mathbf{D}_2\mathbf{E}\|^2 + \gamma_3\|\mathbf{TE}\|^2. \tag{3}$$

The mean of squared residuals is assisted with three terms. The first term is the most important for regularization and possesses the 2nd-order derivative operator $\mathbf{D}_1$ that is defined over three neighboring voxels along each flux tube. The next term is introduced, in imaging, to control spatial roughness perpendicular to the field lines and possesses the 1st-order derivative operator $\mathbf{D}_2$, which is defined for geometrical facility between two neighboring flux tubes. The last term is the proper term of Tikhonov regularization with a diagonal matrix $\mathbf{T}$, which is originally the identity matrix $\mathbf{I}$. The multipliers γ_1, γ_2, and γ_3 are positive-valued and used as parameters for weighting the three terms.

With the extended Lagrangian function, we employ the Cholesky decomposition for numerically reliable minimization. The $\Lambda(\mathbf{E})$ is minimized with respect to $\mathbf{E}$ by solving the following linear equation, which has a unique solution (Appendix A):

$$\left\{\mathbf{L}^T\mathbf{L} + M\gamma_1\left(\mathbf{D}_1{}^T\mathbf{D}_1 + \alpha\mathbf{D}_2{}^T\mathbf{D}_2 + \beta\mathbf{T}^T\mathbf{T}\right)\right\} = \mathbf{L}^T\mathbf{S}, \tag{4}$$

with $\alpha = \gamma_2/\gamma_1$ and $\beta = \gamma_3/\gamma_1$. Since the matrix $\mathbf{P} = \mathbf{D}_1{}^T\mathbf{D}_1 + \alpha\mathbf{D}_2{}^T\mathbf{D}_2 + \beta\mathbf{T}^T\mathbf{T}$ is symmetric and positive definite, the Cholesky decomposition $\mathbf{P} = \mathbf{R}^T\mathbf{R}$ with an upper triangular matrix $\mathbf{R}$ is possible. Then, we have an equation of the conventional form $\left(\mathbf{L}^T\mathbf{L} + M\gamma_1\mathbf{R}^T\mathbf{R}\right)\mathbf{E} = \mathbf{L}^T\mathbf{S}$. With this rewriting, the singular value decomposition (SVD) $\mathbf{LR}^{-1} = \mathbf{U\Sigma V}^T$ leads the solution $\mathbf{E}$ to the ordinary form of series expansion. That is, we have

$$\mathbf{E}(\gamma_1) = \sum_{m=1}^{M} w_m(\gamma_1)\frac{(\mathbf{S}, \mathbf{u}_m)}{\sigma_m}\left(\mathbf{R}^{-1}\mathbf{v}_m\right), \tag{5}$$

with the Tikhonov window

$$w_m(\gamma_1) = \frac{1}{1 + M\gamma_1/\sigma_m{}^2}. \tag{6}$$

With the orthonormal column vectors $\mathbf{u}_m$ and $\mathbf{v}_m$ of the matrices $\mathbf{U}$ and $\mathbf{V}$, one has a basis system $\mathbf{R}^{-1}\mathbf{v}_m$ for $\mathbf{E}(\gamma_1)$ and using the series $\mathbf{u}_m$ as the basis system for $\mathbf{S}$. With the singular values σ_m (diagonal elements of $\mathbf{\Sigma}$) in descending order, one has the monotonically decreasing function $w_m(\gamma_1)$ for tapering down the expansion coefficients $(\mathbf{S}, \mathbf{u}_m)/\sigma_m$, which may

increase in the region of large m (high spatial-frequency); $(\mathbf{a}, \mathbf{b})$ denotes the inner product of vectors $\mathbf{a}$ and $\mathbf{b}$. It should be noted that the inverse of the triangular matrix, $\mathbf{R}^{-1}$, tends to be well-conditioned and calculated numerically with high reliability.

With respect to the solution $\mathbf{E}(\gamma_1)$, the generalized cross-validation (GCV)[22] for optimizing the value of γ_1 is given as

$$\text{GCV}(\gamma_1) = \frac{\varepsilon^2}{\left(1 - M^{-1}\sum_{m=1}^{M} w_m(\gamma_1)\right)^2}, \tag{7}$$

where $\varepsilon^2 = M^{-1}\|\mathbf{LE}(\gamma_1) - \mathbf{S}\|^2$ is the attained mean square error (MSE). Since the matrix $\mathbf{R}$ and thus all the SVD components involve the weights α and β as parameters, the criterion of minimum GCV is valid for particular values of α and β.

The term $\|\mathbf{D}_1\mathbf{E}\|^2$ is defined with the central difference between the second-order differentials along the flux tube. As a boundary condition at both edges of the field lines in the measurement volume, $\nabla_\parallel = 0$ and $\nabla_\parallel^2 = 0$ have been tested with respect to the derivative $\nabla_\parallel$ along field lines. It is found that solutions are almost independent of such boundary conditions. Therefore, in the present analysis, we used the boundary condition $\nabla_\parallel = 0$ for $\|\mathbf{D}_1\mathbf{E}\|^2$. The term $\|\mathbf{D}_2\mathbf{E}\|^2$ is defined with the one-sided difference between the neighboring voxels perpendicular to field lines. The differentiation is introduced along the poloidal direction and along divertor legs, in which directions the flux tubes are stretched by the strong magnetic shear, and thus plasma parameters are expected to be smoothed out due to the parallel transport (Appendix B).

C. Algorithm of image reconstruction

There are two reasons for adding the term $\|\mathbf{TE}\|^2$ in Eq. (3). First, despite the success in Refs. 9–12, the derivative operators such as the Laplacian operator are never well-conditioned in general. In the present scheme of single field-of-view tomography, it is found that the inverse matrix $\mathbf{R}^{-1}$ cannot be calculated without the original Tikhonov term $\|\mathbf{E}\|^2$. Second, the diagonal matrix $\mathbf{T}$ is used for applying the constraint of non-negative valued emissivity. That is, when the initial solution $\mathbf{E}(\gamma_1)$ with the identity matrix $\mathbf{T} = \mathbf{I}$ has negative values at some voxels, we anticipate that the voxels have very low emissivity and, therefore, we set the corresponding diagonal elements $T_{k,k}$ of $\mathbf{T}$ to be large positive values as additional penalties. Then, the voxel values are forced to approach zero in the next iterative step of minimizing the Lagrangian function. With the matrix $\mathbf{T}$ so updated, $\mathbf{R}$ is recalculated at each iteration. Experimentally, it is found that in most of the cases the iteration converges and a reasonable non-negative solution is obtained.

The iterative algorithm of image reconstruction is as follows:

Step 1   Set the values of α and β.
Step 2 $\mathbf{T}^{(0)} = \mathbf{I}$.
Step 3   For $\mathbf{T}^{(n)}$, obtain $\mathbf{R}^{(n)}$, $\mathbf{LR}^{-1(n)}$, and the SVD.
Step 4   Find γ_1 that minimizes $\text{GCV}(\gamma_1)$.
Step 5   For the minimizer γ_1, calculate $\mathbf{E}(\gamma_1)$ according to Eq. (5).
Step 6   For all k where we have $E_k < 0$, set $T_{k,k}{}^{(n+1)}$ to a large value, for example, 10^7. Go to step 3 for $n + 1$.

The procedure from step 3 to step 6 is repeated iteratively until we have no negative-valued new voxels anywhere. With this iteration, the procedure starting with step 1 is repeated in order to find optimum values of α and β, which minimize the reconstruction errors in the test calculation, especially the value of α. The software is interactive only for the choice of α and β. A practical procedure of choosing the α and β values is studied in Sec. III D.

D. Numerical simulations

1. Optimization of regularization parameters

To check the feasibility of tomographic imaging, numerical tests have been conducted. Figure 6 shows one of the tested phantoms, E_{ph}, which imitates emission distribution along the poloidal direction and divertor legs. The emission is nonuniform along flux tubes such that the intensity increased linearly with the distance from the observation point, L_{ph}. In calculation, 1% Gaussian noise with zero mean is added to the projection LE_{ph} for producing the data S, and γ_1 is scanned in a wide range from 10^{-11} to 10^4 for fixed values of α and β. Figure 7 shows an obtained behavior of the GCV, the MSE ε^2, and the reconstruction error δ as functions of γ_1, for a particular series of Gaussian random numbers. Corresponding to the non-uniform voxellation, the error δ is defined as

$$\delta = \frac{\sum_{k=1}^{K} \left| E_{ph,k} - E_k(\gamma_1) \right| V^k}{\sum_{k=1}^{K} V^k}. \tag{8}$$

Here V^k is the own volume of the k-th voxel and has a relation $V^k \geq \sum_{m=1}^{M} V_{m,k}$ with the volumes $V_{m,k}$ which are defined in Eq. (1). Each voxel is not completely contained in the measurement area of fibers. Furthermore, there are spaces among fibers as seen in Fig. 2. The error δ is a quantitative estimate of the deviation of the obtained $E(\gamma_1)$ from the assumed E_{ph} over the entire 3D measurement volume. With the decrease in γ_1, the regularization along flux tubes is weakened by the effect of the Tikhonov window $w_m(\gamma_1)$. As a result, the recovered projection $LE(\gamma_1)$ tends to match precisely the projection data S. The ceiling of ε^2 at $\|E_{ph}\|^2$ for very large γ_1 and the subsequent monotonic decrease in ε^2 seen in Fig. 7 give a proof of correct calculation. On the other hand, the GCV has a minimum around $\gamma_1 = 10^{-5}$, below which the GCV gradually separates from the value of ε^2. The increase in GCV for smaller γ_1, which suggests that the denominator of GCV decreases faster than the numerator, corresponds to the appearance of too fine structure in reconstruction due to too weak regularization.
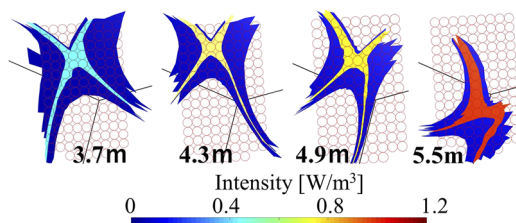

FIG. 6. 3D profile of a phantom. The variation of emissivity along LOS is shown with cross-sectional illustrations at different L_{dp}. Red circles in each panel indicate the fiber positions.

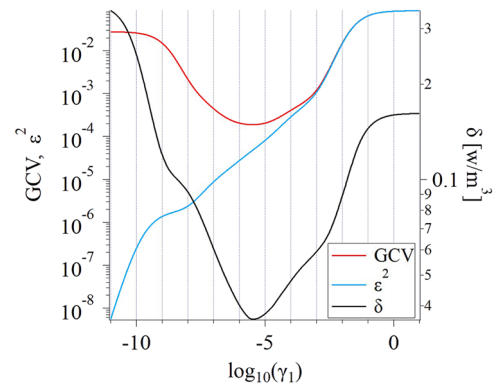FIG. 7. Behaviors of GCV, ε^2, and δ when the parameter γ_1 is changed for fixed values of $\alpha = 10^{-2}$ and $\beta = 10^{-6}$.

As expected, the minimum of GCV agrees well with the minimum of the reconstruction error.

This result of reconstruction in Fig. 7 has been obtained for $\alpha = 10^{-2}$ and $\beta = 10^{-6}$. When the test is made in the range of $10^{-5} \leq \alpha \leq 10^{-1}$ and $10^{-6} \leq \beta \leq 10^{-2}$, the $E(\gamma_1)$ obtained with the criterion of minimum GCV is not changed significantly by the value of β. Therefore, β can be fixed at such a small value of the level that is indispensable for sure calculation of R^{-1}. However, the change in α gives a significant change in reconstruction. Considering that the minimum of GCV for a set of (γ_1, α) seems to indicate the minimum of δ in many tests, the value of α is selected as such without support of statistical mathematics, $\alpha = 10^{-2}$ in this example. Recalling that these values of α and β are the weights in ratio among three regularization terms in Eq. (3), we note that the very small value $\beta = 10^{-6}$ should also be related to the magnitude of the squared norm $\|E\|^2$, which is much larger than those of the two derivatives. Additionally, for phantoms where the emissivity distribution is local and narrow in the flux-tube direction, the best value of γ_1 has tended to decrease. Based on these simulation results, the scans of γ_1, α, and β are efficiently made in narrowed ranges for the rest of the analyses.

2. Regularization effects in reconstructed images

The two derivative terms $\|D_1 E\|^2$ and $\|D_2 E\|^2$ give meaningful effects to the profiles of reconstructed images. In the simulations, the reconstruction is studied for changing the regularization term design.

First, comparison is made in two cases of using only the Tikhonov term $\|TE\|^2$ and using all three terms. Figures 8 and 9 show a result in the simulation for which the result in Fig. 7 was obtained. With similarly good fittings to the phantom projection as recognized in Fig. 8, the two methods give reconstructions with a remarkable difference as in Figs. 9(a) and 9(b), where both the phantom in Fig. 6 and the reconstructed images are raster-scanned and plotted in one dimension. In this plot of $E_{ph,k}$, the phantom profile is discontinuous in its existence intervals and oscillates like saw teeth corresponding to the linear increase in emissivity with L_{dp}. With the two derivative terms and the optimization with GCV, it is found that the reconstruction is much improved in giving a better recovery of the gradient of phantom along flux tubes and the noisy structure effectively diminished. The iterative
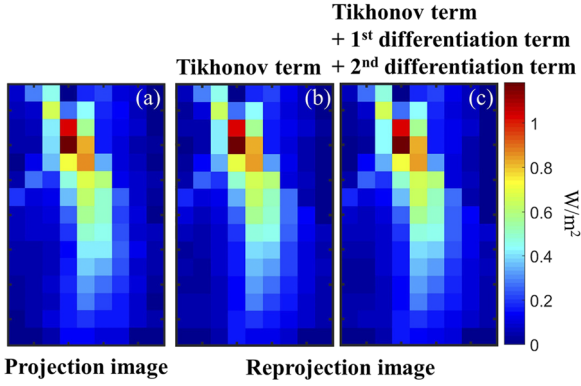
FIG. 8. (a) Projection image of the phantom with no noise; those recovered with (b) the Tikhonov term only and (c) all terms.

procedure for non-negativity, with 14 iterations in this example, has worked well without producing any large residual. The iterative update of the operator **T**, which has worked well also in the case of the single term $\|\mathbf{TE}\|^2$, can be a tool for eliminating the noisy negative values that appear in the original Tikhonov regularization.[23,24] The tool is available wherever one has the linear regularization software.

In Fig. 10, the reconstructed images are illustrated for some of the various regularization designs. The numerical sequences (red lines) in Figs. 9(a) and 9(b) are displayed in Figs. 10(a) and 10(d), now with cross-sectional illustrations at different L_{dp}. Here we tested also the assumption of constant emission along field lines in order to see how the result deviates from that with the regularizations of the parallel derivative term $\|\mathbf{D}_1\mathbf{E}\|^2$. The resulting image is plotted in Fig. 10(b). The reconstruction so-modified is made simply by decreasing the size of **E** to the number of flux tubes and summing the related row vectors of the projection matrix **L**. Evidently, the flux constant constraint can never give good effects as the result of imposing an excessive claim on the reconstruction.
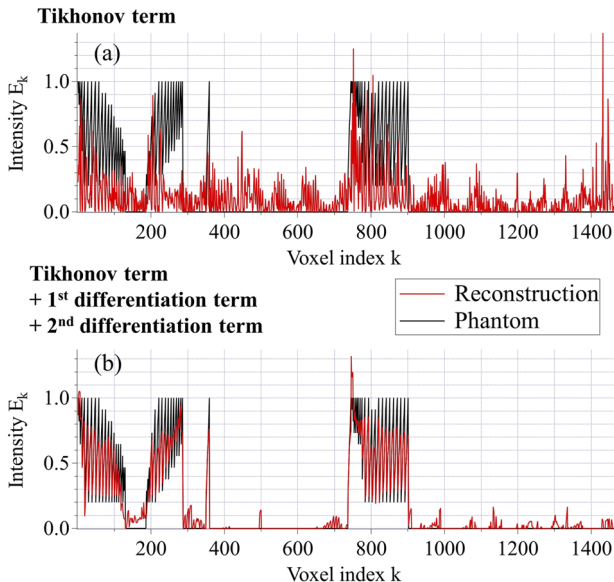

FIG. 9. 1D display of the phantom and the images reconstructed with (a) the Tikhonov term only and (b) all terms. 1464 voxels are indexed in sequence by raster scan along the LOS of fibers.
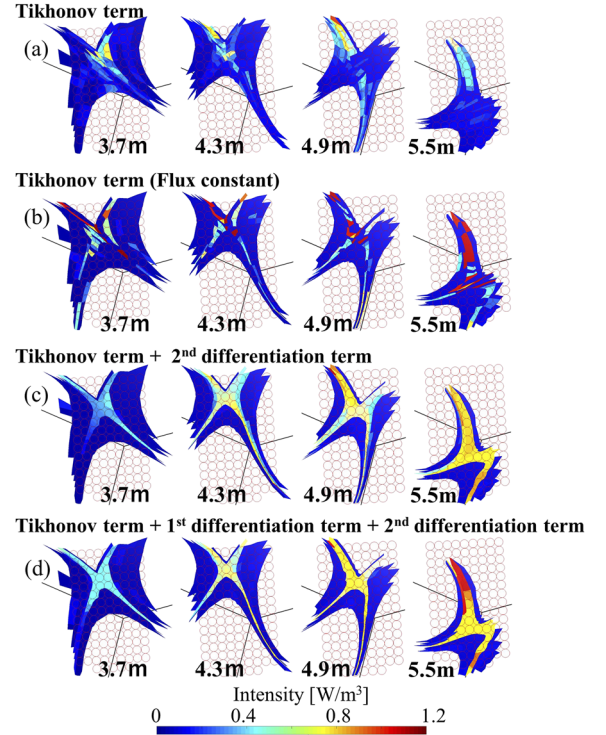

FIG. 10. Reconstructed images for different designs of regularization: (a) $\|\mathbf{TE}\|^2$ only $\left(\delta = 1.8 \times 10^{-1}\right)$, (b) $\|\mathbf{TE}\|^2$ with the constraint of flux constant $\left(\delta = 3.0 \times 10^{-1}\right)$, (c) $\|\mathbf{TE}\|^2$ and $\|\mathbf{D}_1\mathbf{E}\|^2$ $\left(\delta = 7.1 \times 10^{-2}\right)$, and (d) all terms $\left(\delta = 3.6 \times 10^{-2}\right)$.

By contrast, the addition of $\|\mathbf{D}_2\mathbf{E}\|^2$ term improves the reconstruction clearly, as shown in Fig. 10(c).

The reconstruction is further improved by adding the term $\|\mathbf{D}_2\mathbf{E}\|^2$ as seen in Fig. 10(d), where the reconstruction error δ is decreased.

3. Regularization effects in numerical components

The improved image displayed in Figs. 9(b) and 10(d) is examined on its spectral components, which are given a significant change by applying the two derivative terms.

In Fig. 11 are exhibited the singular value series, the Tikhonov window, the spectral coefficients, and the coupling of basis systems, which were used to calculate the image according to Eq. (5). The σ_m as well as w_m gradually decrease with increasing m. The spectral coefficients of **S** and $\mathbf{E}(\gamma_1)$ in Figs. 11(b) and 11(c) are compressed nicely in the region of low spatial-frequency (small number m), especially at m = 1. This compression is supported by the basis systems that are displayed in Figs. 12 and 13. The bases $\mathbf{R}^{-1}\mathbf{v}_m$ for $\mathbf{E}(\gamma_1)$ change in profile with the increase in *m* from smooth to random functions. In particular, the basis $\mathbf{R}^{-1}\mathbf{v}_1$ has a distribution that is similar to the emission region in shape and thereby supports the strong spectral compression of $\mathbf{E}(\gamma_1)$ at m = 1 and the related smooth profile seen in Fig. 10(d). The great profile change in $\mathbf{R}^{-1}\mathbf{v}_m$ in the interval of $1 \leq m \leq M$ suggests that the basis system can support various emissivity distributions, occasionally with fine structures. On the contrary, the regularization only with $\|\mathbf{TE}\|^2$ fails in generation of smooth bases for small m and, as a result, gives the unstable profile of emissivity, as
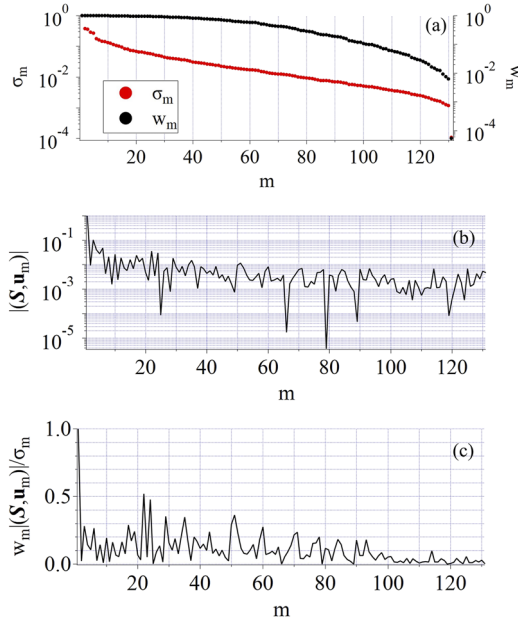
FIG. 11. (a) Singular value series σ_m normalized with σ_1 and the window function w_m, (b) the spectrum of data **S**, and (c) the normalized spectrum of the image $\mathbf{E}(\gamma_1)$ obtained with all regularization terms ($\gamma_1 = 10^{-5}$, $\alpha = 10^{-2}$, and $\beta = 10^{-6}$).

seen in Fig. 10(a). This notable improvement of the basis system has been obtained by involving the derivative terms in regularization.

The above results have been obtained with the **T**-iteration for non-negativity and with the GCV-optimization according to the previously described algorithm. In Figs. 10(b) and 10(d), the spectral coefficients are plotted in magnitude for graphic convenience. Calculation was carried out with the software Matlab. To obtain the result of, for example, Fig. 10(d), computing time with 14 iterations is 50 s using the Intel® Core™ i7-6700K without sparse matrix acceleration.[25]
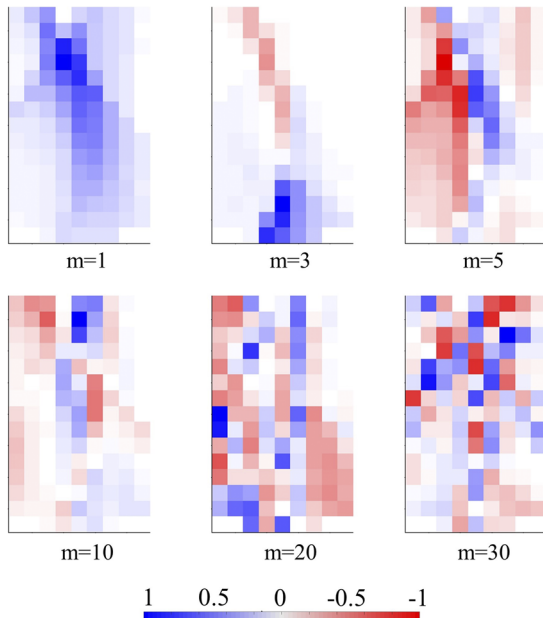

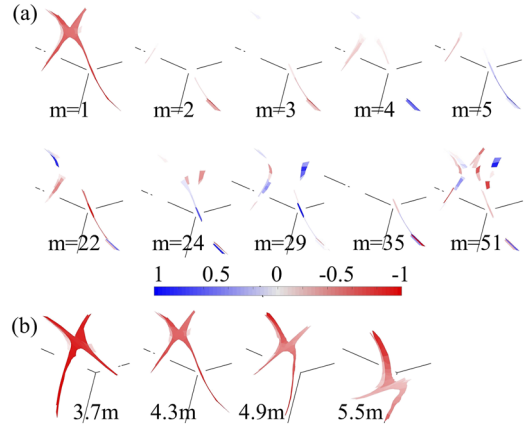FIG. 12. Bases $\mathbf{u}_m$ for the spectral decomposition in Fig. 10(b).

FIG. 13. Bases $\mathbf{R}^{-1}\mathbf{v}_m$ for the spectral decomposition in Fig. 11(c): (a) cross-sectional display for various m (L_{dp} = 4.3 m), where each basis is normalized with its maximum value. (b) Cross sections of $\mathbf{R}^{-1}\mathbf{v}_1$ at different L_{dp}. The inversion in color-bar is in correspondence with the sign inversion of the spectrum in Fig. 11(c).

IV. APPLICATION TO IMPURITY EMISSIONS IN THE LHD EDGE REGION

Impurity emissions in the LHD experiments, CII($1s^22s2p3s\ ^4P^o$-$1s^22s2p3p\ ^4P$, 514 nm) and CIV($1s^25f\ ^2F^o$-$1s^26g\ ^2G$, $1s^25g\ ^2G$-$1s^26h\ ^2H^o$, 466 nm), are analyzed with the tomography method described above. Figure 14 shows CII and CIV projection images at the detector and the recovered images in tomography. Here we have $n_e = 2 \times 10^{19}$ m^{-3}, NBI heating power of 13 and 14 MW, shot numbers 133 323 and 137 177, t = 4.75 and 4.30 s, exposure time = 0.15 and 0.30 s, gratings of 150 and 2400 grating/mm, respectively, for CII and CIV measurements ($\gamma_1 = 2.6 \times 10^{-6}$, 1.0×10^{-6}; $\alpha = 10^{-3}$, $\beta = 10^{-6}$). The selection of α is based on the analysis as follows. Before
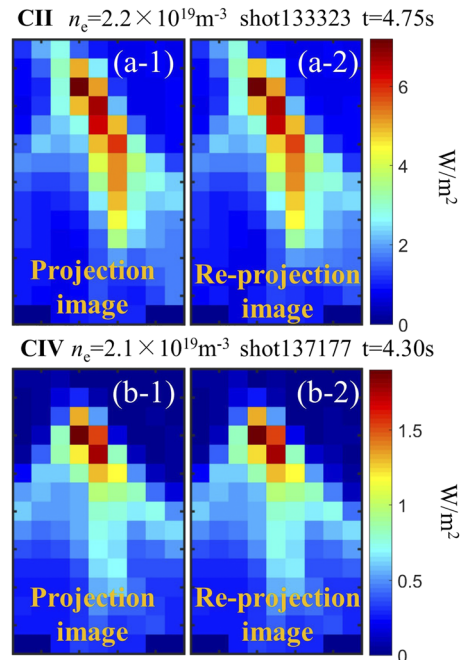

FIG. 14. (a) Projection data in the LHD experiment and (b) the recovered projections for CII and CIV.

the application to the experimental data, we have tested several different phantoms with emission distributed only along LCFS and only localized around the X-point in addition to the one shown in Fig. 6. We have found that the optimum value of α, which gives minimum δ, changes from 10^{-4} to 10^{-2} in the tests depending on the emission distributions. Based on the tests, we have selected $α = 10^{-3}$ for the analysis of experimental data. The reconstructed 3D images are shown in Fig. 15 at different distances from the detector, L_{dp}. In reconstruction, the emissions are peaked at the left divertor leg of L_{dp} = 5.5 m for both CII and CIV. This is considered due to strong plasma-wall interaction caused by divertor shaping at the top of the torus that terminates the divertor leg field lines with a rather large incident angle. The emission of CIV is found to peak around the X-point and is also distributed in the poloidal direction with a certain modulation. On the other hand, there exists no clear peak in the CII emission except for the left leg. These differences between CII and CIV emission distributions are probably attributed to different ionization potentials, 24.4 eV for CII and 64.7 eV for CIV. That means CIV emission occurs in a higher temperature region.

Based on this experimental result, the following point may be noted for application and improvement of the tomography method for the edge plasma. In the edge region, strongly peaked emissions can exist especially near the divertor plates due to strong plasma-wall interaction, as also observed in the present analysis. In this case, reconstruction needs basis functions with high orders m to reproduce such peaked distributions. The basis functions with higher m, on the other hand, have the potential to increase the spatial oscillation of emission by amplifying noise components and thus tend to be suppressed by the window function. Therefore, the selection of regularization parameters that control smoothness of the solution should be made carefully by considering possible peaks appearing near plasma-facing components. In order to avoid any misleading reconstruction caused by the peaked distributions, separation of the control volume with possible peaked

solution from the others in tomography analysis may be one solution.

V. SUMMARY

A single field-of-view tomography method has been proposed for inverting the impurity emission distributions measured in magnetized edge plasma. Several regularization terms have been introduced taking into account the plasma transport characteristics in the magnetized plasma, in addition to the conventional Tikhonov regularization. The new scheme has been tested with the phantom data that vary the emissivity along the field line direction. The effectiveness of the regularization terms has been confirmed in regard to the reconstruction error that can be reduced with the introduced regularization of derivative operators parallel and perpendicular to the magnetic field lines. In the test, the selection of regularization parameter values has also been discussed. It is found that the test image is effectively compressed to the Fourier-type components of low order, m = 1 and around m = 20. The scheme has been applied to the experimental data in LHD. Different distributions are obtained for CII (C^{1+}) and CIV (C^{3+}), which seem reasonable in terms of ionization potentials of each charge state and of the plasma-wall interaction. Special care should be taken for tomography analysis in the edge plasma, where strongly peaked emission can exist due to plasma-wall interaction, which may conflict with regularizations that usually promote smooth distribution of solutions.

APPENDIX A: EXTENDED LEAST-SQUARES SOLUTION

Equation (4) can be obtained from $\partial\Lambda(\mathbf{E})/\partial E_k$ (k = 1, 2, . . . , K) on the convex function $\Lambda(\mathbf{E})$. But an efficient procedure is as follows. As well known, the minimizer of $\|\mathbf{LE} - \mathbf{S}\|^2$ (i.e., the lest-squares solution of $\mathbf{LE} = \mathbf{S}$) is the solution of the normal equation $\mathbf{L}^T\mathbf{LE} = \mathbf{L}^T\mathbf{S}$. Noting the relation

$$\left\|\begin{pmatrix}\mathbf{a}\\\mathbf{b}\end{pmatrix}\right\|^2 = \begin{pmatrix}\mathbf{a}\\\mathbf{b}\end{pmatrix}^T\begin{pmatrix}\mathbf{a}\\\mathbf{b}\end{pmatrix} = \mathbf{a}^T\mathbf{a} + \mathbf{b}^T\mathbf{b} = \|\mathbf{a}\|^2 + \|\mathbf{b}\|^2 \quad (A1)$$

for column vectors $\mathbf{a}$ and $\mathbf{b}$, one can rewrite Eq. (3) as

$$\Lambda(\mathbf{E}) = \frac{1}{M}\left\|\begin{pmatrix}\mathbf{L}\\M\gamma_1\mathbf{D}_1\\M\gamma_2\mathbf{D}_2\\M\gamma_3\mathbf{T}\end{pmatrix}\mathbf{E} - \begin{pmatrix}\mathbf{S}\\0\\0\\0\end{pmatrix}\right\|^2 = \frac{1}{M}\|\bar{\mathbf{L}}\mathbf{E} - \bar{\mathbf{S}}\|^2, \quad (A2)$$
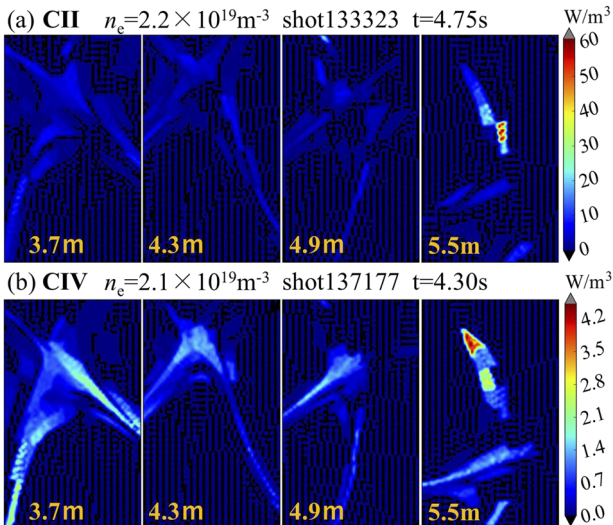

FIG. 15. Reconstructed images of (a) CII and (b) CIV in the cross-sectional display at different L_{dp}.

with the K-dimensional zero vector 0. With the enlarged coefficient matrix $\bar{\mathbf{L}}$ and data vector $\bar{\mathbf{S}}$, the minimization of $\Lambda(\mathbf{E})$ is reduced to minimizing $\|\bar{\mathbf{L}}\mathbf{E} - \bar{\mathbf{S}}\|^2$. The corresponding normal equation $\bar{\mathbf{L}}^{\mathrm{T}}\bar{\mathbf{L}}\mathbf{E} = \bar{\mathbf{L}}^{\mathrm{T}}\mathbf{S}$ is deployed as Eq. (4) by simple matrix manipulation.

APPENDIX B: FORMS OF D₁ AND D₂

The operator $\mathbf{D}_1$, the second order derivative along the field line that consists of 5 voxels, e.g., from $k - 2$ to $k + 2$, as shown in Fig. 5, can be written as

$$\frac{1}{dl^2}\begin{pmatrix}\ddots & & & & & \\ & -1 & 1 & 0 & 0 & 0 \\ & 1 & -2 & 1 & 0 & 0 \\ & 0 & 1 & -2 & 1 & 0 \\ & 0 & 0 & 1 & -2 & 1 \\ & 0 & 0 & 0 & 1 & -1 \\ & & & & & & \ddots \end{pmatrix}$$

where dl is the distance between neighboring planes perpendicular to the line of sight, l and $l + 1$. The derivative constitutes a 5×5 cluster in the matrix $\mathbf{D}_1$, which has a size of $K \times K$ with K being the total number of voxels. The derivative is defined as the central difference except for the edges of the field lines ($k - 2$ and $k + 2$ in this case), where $\nabla_{\parallel} = 0$ is assumed.

On the other hand, the first order derivative perpendicular to the field line, $\mathbf{D}_2$, with one-sided difference, is written as

$$\begin{pmatrix}\ddots & & & & & & \vdots & & & & & \vdots & & & & & \\ & 0 & dl^{-1}_{k-1,k-6} & 0 & 0 & 0 & 0 & -dl^{-1}_{k-1,k-6} & 0 & 0 & 0 & 0 & 0 & 0 & 0 & 0 \\ & 0 & 0 & 0 & 0 & 0 & 0 & -dl^{-1}_{k-1,k+4} & 0 & 0 & 0 & 0 & dl^{-1}_{k-1,k+4} & 0 & 0 & 0 \\ & & & & & & \vdots & & & & & \vdots & & & & & \\ & 0 & 0 & dl^{-1}_{k,k-5} & 0 & 0 & 0 & 0 & -dl^{-1}_{k,k-5} & 0 & 0 & 0 & 0 & 0 & 0 & 0 \\ & 0 & 0 & 0 & 0 & 0 & 0 & 0 & -dl^{-1}_{k,k+5} & 0 & 0 & 0 & 0 & dl^{-1}_{k,k+5} & 0 & 0 \\ & & & & & & \vdots & & & & & \vdots & & & & & \ddots \end{pmatrix},$$

where $dl_{k,k+1}$ represents the distance between the center of gravities of the voxels k and k + 1. The first line shown in the matrix represents the derivative between the voxels of $k - 6$ and $k - 1$, and the second line represents that between $k - 1$ and $k + 4$, respectively, as shown in Fig. 5. The similar operations are applied for the voxels k, $k - 5$, and $k + 5$ as defined in the fourth and fifth lines in the shown matrix. Then, the number of columns of $\mathbf{D}_2$ is the total number of voxels, K, and the number of lines is the number of derivatives defined in the calculations.

[1]M. Kobayashi *et al.*, Nucl. Fusion **55**, 104021 (2015).
[2]N. Ohyabu *et al.*, Nucl. Fusion **34**, 387 (1994).
[3]Y. Feng *et al.*, Nucl. Fusion **48**, 024012 (2008).
[4]M. Kobayashi *et al.*, Nucl. Fusion **53**, 093032 (2013).
[5]M. Kobayashi *et al.*, Nucl. Mater. Energy **12**, 1043 (2017).
[6]T. Kobayashi *et al.*, Plasma Fusion Res. **13**, 3402030 (2018).
[7]S. Morita *et al.*, Plasma Phys. Controlled Fusion **56**, 094007 (2014).
[8]M. Kobayashi *et al.*, Rev. Sci. Instrum. **88**, 033501 (2017).
[9]N. Iwama *et al.*, Appl. Phys. Lett. **54**, 502 (1989).
[10]N. Iwama, in *Tomography for Discharge Plasmas*, edited by K. H. Becker *et al.* (AIP Press, New York, 1996), pp. 289–298.
[11]N. Terasaki, Y. Hosoda *et al.*, Fusion Eng. Des. **34-35**, 801 (1997).
[12]S. Ohdachi *et al.*, Plasma Sci. Technol. **8**, 45 (2006).
[13]L. Dong *et al.*, Rev. Sci. Instrum. **84**, 083506 (2013).
[14]A. Wingen *et al.*, J. Comput. Phys. **289**, 83 (2015).
[15]J. Bielecki *et al.*, Rev. Sci. Instrum. **86**, 093505 (2015).
[16]M. Anton, H. Weisen *et al.*, Plasma Phys. Controlled Fusion **38**, 1849 (1996).
[17]J. Mlynar *et al.*, Fusion Sci. Technol. **58**, 733 (2010).
[18]M. Odstrcil, J. Mlynar *et al.*, Nucl. Instrum. Methods Phys. Res., Sect. A **686**, 156 (2012).
[19]J. M. Gao, Y. Liu *et al.*, Rev. Sci. Instrum. **84**, 093503 (2013).
[20]N. Iwama *et al.*, J. Plasma Fusion Res. **8**, 691 (2009).
[21]A. S. Jacobson, L. Stagner, M. Salewski, B. Geiger, W. W. Heidbrink, S. B. Korsholm, F. Leipold, S. K. Nielsen, J. Rasmussen, M. Stejner, H. Thomsen, M. Weiland, and ASDEX Upgrade Team, Plasma Phys. Controlled Fusion **58**, 045016 (2016).
[22]G. H. Golub, M. Heath, and G. Wahba, Technometrics **21**, 215 (1979).
[23]R. Sano *et al.*, Rev. Sci. Instrum. **87**, 053502 (2016).
[24]R. Sano *et al.*, Rev. Sci. Instrum. **87**, 11D440 (2016).
[25]T. Odstrčil, T. Pütterich, M. Odstričil, A. Gude, V. Igochine, U. Stroth, and ASDEX Upgrade Team, Rev. Sci. Instrum. **87**, 123505 (2016).